LANGMUIR

pubs.acs.org/Langmuir Article

Antibacterial Activity of Nitrogen-Doped Carbon Dots Enhanced by Atomic Dispersion of Copper

Forrest Nichols, Jia En Lu, Rene Mercado, Mauricio D. Rojas-Andrade, Shunlian Ning, Zahra Azhar, Jasleen Sandhu, Rafael Cazares, Chad Saltikov,* and Shaowei Chen*

Cite This: *Langmuir* 2020, 36, 11629–11636 Read Online

ACCESS | Metrics & More | Article Recommendations | Supporting Information

ABSTRACT: Antibiotic resistance is an imminent threat to human health, requiring the development of effective alternate antibacterial agents. One such alternative includes nanoparticle (photo)catalysts that are good at producing reactive oxygen species (ROS). Herein, we report the design and preparation of nitrogen-doped carbon dots functionalized with atomically dispersed copper centers by Cu−N coordination (Cu/NCD) that exhibit apparent antibacterial activity toward Gram-negative *Escherichia coli* (*E. coli*) under photoirradiation. The growth of *E. coli* cells is found to be markedly inhibited by Cu/NCD under 365 nm photoirradiation, whereas no apparent inhibition is observed in the dark or with the copper-free carbon dots alone. This is ascribed to the prolonged photoluminescence lifetime of Cu/NCD that facilitates the separation of photogenerated electron−hole pairs and ROS formation. The addition of *tert*-butyl alcohol is found to completely diminish the antimicrobial activity, suggesting that hydroxyl radicals are responsible for microbial death. Consistent results are obtained from fluorescence microscopic studies using CellROX green as the probe. Similar bactericidal behaviors are observed with Gram-positive *Staphylococcus epidermidis* (*S. epidermidis*). The copper content within the carbon material is optimized at a low loading of 1.09 wt %, reducing the possibility of toxic copper-ion leaching. Results from this study highlight the significance of carbon-based nanocomposites with isolated metal species as potent antimicrobial reagents.

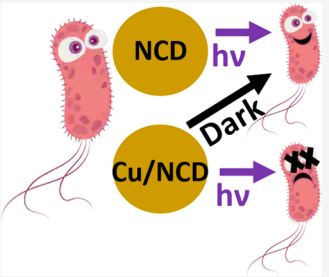

INTRODUCTION

Antibiotic resistance is on the rise and considered one of the greatest health threats facing humanity.[1−4] β-Lactam antibiotics are the most frequently prescribed antibiotics in hospital settings; however, this type of antibiotics is shown to become easily resisted by bacteria through bacterial enzymes known as β-lactamases.[5] Although researchers have provided short-term mechanisms to overcome this type of antibacterial resistance, the use of such antibiotics is proving to be an uphill and losing battle.[5] Significant research has therefore been dedicated to developing alternate antibiotic agents that can overcome bacterial resistance through unique bactericidal pathways. One such alternate route includes the use of light-sensitive nanomaterials capable of producing destructive reactive oxygen species (ROS), such as superoxide (O_2^-), singlet oxygen ($O_2^{\bullet}$), hydroxyl radical ($^{\bullet}OH$), and hydrogen peroxide (H_2O_2).[6−8] The mechanism of attack involves various destructive pathways, such as the degradation of bacterial DNA and bacterial cell membrane.[9] It is inherently difficult for bacteria to overcome such destructive mechanisms of attack and therefore less likely for the bacteria to resist ROS-generating nanomaterials. Toward this end, graphene derivatives represent a unique functional nanomaterial.[10−17] In a recent study,[18] we examined and compared the bactericidal activity of graphene oxide quantum dots before and after chemical reduction and found that the oxidized forms were preferred for improved antibacterial activity under UV photoirradiation. This was attributed to oxygenated structural defects within the graphene oxide quantum dots that led to the ready production of ROS under photoexcitation.

Copper-based photocatalysts have also been rather extensively studied for their ability to produce ROS upon photoirradiation.[19−30] However, the materials used in these studies typically contain high levels of copper, which can cause leaching of copper ions and devastating biological effects including copper toxicity.[31] To facilitate ROS production and concurrently prevent uncontrolled ion leaching, metal loading should be minimized and stabilized but without compromising the antibacterial efficiency. One route to this end involves metal species atomically dispersed within carbon-based support materials. For example, Gong et al.[32] observed ROS production by atomically dispersed gold−carbon dots and found that the optimal Au loading of 15.3 wt % resulted in nearly complete glutathione degradation, owing to high Au atomic dispersion. When the Au loading was increased to 45.7 wt % and large Au nanoparticles were formed, glutathione degradation was found to decrease. The increased activity by

Received: August 4, 2020
Revised: September 11, 2020
Published: September 14, 2020

https://dx.doi.org/10.1021/acs.langmuir.0c02293
Langmuir 2020, 36, 11629−11636

the material containing single Au atoms was attributed to mitochondrial targeting, glutathione depletion, and ROS production within bacterial membranes. Such atomic dispersion of metals can be readily realized with nitrogen-doped carbon dots by, for instance, a facile wet impregnation procedure with the formation of metal−nitrogen coordination linkages.[33,34] The surface enrichment of the active metal centers can lead to the effective production of ROS due to enhanced separation and migration of the photogenerated electron−hole pairs.[35−37] This unique feature may be exploited for the development of high-performance antimicrobial reagents, in comparison to the conventional homogeneous organometallic complexes. This is the primary motivation of the present work.

Herein, nitrogen-doped carbon dots with atomically dispersed copper (Cu/NCD) were prepared by a solid-state thermal route. The copper content was found to be around 1 wt % in all samples. Transmission electron microscopy (TEM) and elemental mapping measurements suggest atomic dispersion of copper within the carbon matrix by the formation of Cu−N bonds, as manifested in X-ray photoelectron spectroscopy (XPS) measurements. Steady-state photoluminescence (SSPL) measurements showed that the emission was markedly quenched with the incorporation of copper into the carbon dots, consistent with the increased lifetime as observed in time-resolved photoluminescence (TRPL) measurements. The bactericidal activity of the obtained composites was then tested using Gram-negative *Escherichia coli* as the initial illustrating example. It was found that the bacterial growth was apparently inhibited under 365 nm photoirradiation, whereas no inhibition was observed in the dark, and the inhibition activity increased with increasing sp^2 carbon content in the sample, possibly due to improvement in electron−hole migration. Consistent results were obtained in scanning electron microscopy (SEM) measurements of the bacterial cell morphologies. In addition, the bactericidal activity was found to diminish markedly upon the addition of *tert*-butyl alcohol, suggesting that hydroxy radicals were responsible for the antimicrobial activity, which was further confirmed in fluorescence microscopic measurements using CellROX green as the probe. A similar bactericidal performance was observed with Gram-positive *Staphylococcus epidermidis*.

EXPERIMENTAL SECTION

Chemicals. Melamine (99%, Acros Organics), citric acid anhydrous (Certified ACS, Fisher Chemicals), copper(II) acetylacetonate ($Cu(acac)_2$, 98%, Acros Organics), phosphate-buffered saline tablets (PBS, Acros Organics), sodium chloride (NaCl, Fisher Chemicals), yeast extract (Fisher BioReagents), agar (Fisher BioReagents), *tert*-butyl alcohol (TBA, ≥99.5%, Sigma-Aldrich), tryptone (Fisher BioReagents), and CellROX green (ThermoFisher) were used as received. All solvents were obtained through typical commercial sources and used without further purification. Water was supplied by a Barnstead Nanopure water system (18.3 MΩ cm).

Characterizations. TEM measurements were performed on a JOEL JEM 2100F microscope. UV−vis measurements were performed on a PerkinElmer Lambda 35 UV−vis spectrometer with a scan rate of 240 nm min^{-1} and a slit width of 1 nm. SSPL measurements were performed on a PTI fluorospectrometer. TRPL spectra were acquired using a Horiba QM-3304 instrument at a pulsed laser excitation of 337 nm in the time-correlated single-photon counting (TCSPC) mode. XPS measurements were performed with a Phi 5400/XPS instrument equipped with an Al Kα source operated at 350 W and 10^{-9} Torr. X-ray diffraction (XRD) measurements were conducted on a Rigaku Smartlab Powder and thin-film diffractometer with Cu Kα (λ = 1.54 Å) radiation. Inductively coupled plasma-optical emission spectrometry (ICP-OES) measurements were carried out with a PerkinElmer Optima instrument.

Synthesis of Nitrogen-Doped Carbon Dots with Atomically Dispersed Copper. The samples were prepared by adopting a solid-state method reported previously.[38] Briefly, citric acid (0.8 g), melamine (1.6 g), and $Cu(acac)_2$ (0, 0.25, 0.5, or 1.0 mmol) were mixed into a homogeneous powder by a mortar and pestle. The solid was then added into a Teflon-lined autoclave and heated to 180 °C for 5 h. Under these reaction conditions, citric acid and melamine underwent dehydration reactions to produce nitrogen-doped carbon dots.[38] $Cu(acac)_2$ was chosen for its thermal stability. Once cooled to room temperature, the Teflon liner was opened, and the product was dispersed in water by sonication. The dispersion was centrifuged at 6000 rpm for 10 min to remove insoluble aggregates. The resulting brown supernatant was purified with a dialysis membrane (3.5 K MWCO) for 72 h, condensed through rotary evaporation, and dried in a vacuum oven at 60 °C overnight. For the sample prepared in the absence of $Cu(acac)_2$, it was hereon referred to as NCD, whereas those with the addition of an increasing feed of $Cu(acac)_2$ as Cu/NCD-1, Cu/NCD-2, and Cu/NCD-3, respectively.

Preparation of Bacterial Suspension. *E. coli* (ATCC 25922) and *S. epidermidis* (ATCC 12228) streaked on sterile Luria−Bertani (LB) agar plates were incubated overnight at 37 °C. A single colony was selected and inoculated in sterile LB (3 mL) at 37 °C for 18 h with shaking. The resulting liquid culture was centrifuged at 8000 rpm for 1 min, followed by washing with sterile 1× PBS three times. The resulting bacterial suspension was diluted to an optical density (OD) of 0.1 at 600 nm and used in the following antibacterial experiments.

Bacterial Growth in the Dark. Bacterial growth in the dark was monitored using a sterile 96-well plate with a final volume of 200 μL in each well. NCD or Cu/NCD (120 μg) was loaded into each well through serial dilution of a 1 mg mL^{-1} stock solution in 1× PBS to obtain a final concentration of 600 μg mL^{-1}. The previously prepared bacterial suspension (40 μL, 0.1 OD) was added to each well to obtain identical starting bacterial concentrations to those in the photocatalytic studies (below). LB (20 μL) was added to each well and the wells were incubated at 37 ° for 24 h, with data collection performed at 600 nm in 2 min intervals.

Photocatalytic Antibacterial Studies. Photocatalytic antimicrobial measurements were performed using a modified method adopted from previous reports.[17,39] Briefly, NCD and Cu/NCD solutions (1 mg mL^{-1}) were prepared by dissolving purified samples in 1× PBS. This solution (600 μL) was added to a 1.5 mL centrifuge tube. A bacterial suspension (200 μL, 0.1 OD) of either *E. coli* or *S. epidermidis* was added to each sample tube, and the final volume was brought to 1 mL using 1× PBS to obtain a final NCD or Cu/NCD concentration of 600 μg mL^{-1}. After photoirradiation (100 W, 1000−1500 lumen with a peak emission of 365 nm, Dongguan Hongke Lighting Co., China) for a varied period of time (up to 7 min), 100 μL of the resulting solution was taken and diluted by a factor of 10^{-2}. The diluted solution (10 μL) was dropped onto an LB agar plate and dispersed using sterile glass beads. The resulting LB agar plates were grown for 18 h at 37 °C in a dark incubator. The colony-forming units (CFUs) on each plate were counted and recorded as a function of time. These experiments were repeated for a total of three times to produce time point averages and standard deviations.

To test the formation of hydroxyl radicals, TBA (10 μL, 1 g L^{-1}) was added to the suspension before dilution to a final volume of 1 mL with 1× PBS. This gave a TBA concentration of 10 mg L^{-1} during the photodynamic experiments.

Scanning Electron Microscopy Studies. SEM images of the bacterial cell morphologies were acquired with an FEI Quanta 3D field-emission scanning electron microscope. For the control experiment, 100 μL of *E. coli* suspension (0.1 OD in 1× PBS) was drop-cast onto a sterile glass slide in the dark. The droplet was set to dry just at the edges for approximately 15 min before serial washing in solutions of 10, 25, 50, 75, 90, and 100% ethanol to dehydrate the sample. Once in 100% ethanol, the sample was placed in a critical point dryer (CPD) where ethanol was exchanged with CO_2. The fully dried

https://dx.doi.org/10.1021/acs.langmuir.0c02293
Langmuir 2020, 36, 11629−11636

sample was then sputtered with gold to improve the contrast and resolution during SEM imaging. Two more samples were prepared in the same manner but in the presence of Cu/NCD-3, one in the dark and the other under photoirradiation at 365 nm for 7 min.

Fluorescence Microscopy Studies. The bacterial suspensions (300 μL), prepared as previously described, were added to centrifuge tubes and diluted to 1 mL using either PBS alone, NCD in PBS, or Cu/NCD-3 in PBS to obtain a final nanoparticle concentration of 600 μg mL^{-1}. These centrifuge tubes were irradiated with light (395−400 nm) positioned 10 cm above the light base for 1 min. CellROX green (1.8 μL, 2.5 mM in dimethyl sulfoxide (DMSO)) was added to each of the resulting irradiated centrifuge tubes to obtain a final concentration of 25 μM and incubated for 10 min at 37 °C. CellROX green-stained cell suspension (1 μL) was added to an agar pad (1 cm^2, 1% H_2O). Fluorescence images were collected using 470 ± 40 nm excitation and 525 ± 50 nm emission filters, a 63× water immersion lens, and three regions of interest (ROIs) per sample. The integrated fluorescence intensity after background subtraction was averaged across the three ROIs.

RESULTS AND DISCUSSION

The successful production of carbon dots was first confirmed by TEM measurements. From Figure 1a, one can see that for the copper-free sample (NCD), carbon dots are very well dispersed without apparent agglomeration, with a roughly spherical shape, most likely due to abundant oxygenated functional moieties on the carbon dot surface that rendered them soluble in water, as observed previously.[35,36] Statistical analysis based on ca. 100 nanoparticles shows that the particle size falls mostly in the range of 12−37 nm, with an average of 22.8 ± 7.2 nm, as manifested in the core size histogram in Figure S1. For the copper-containing carbon dots, the morphologies remained virtually invariant, as evidenced with Cu/NCD-3 in Figure 1b, which shows a somewhat smaller average core size of 15.8 ± 3.0 nm. Notably, high-resolution TEM measurements of both samples show no well-defined lattice fringes (Figure S2) that can be ascribed to either carbon or copper (oxide), suggesting only short-range ordering of the carbon skeletons into which copper was most likely atomically dispersed. Consistent results are obtained in elemental mapping measurements (Figure S3).

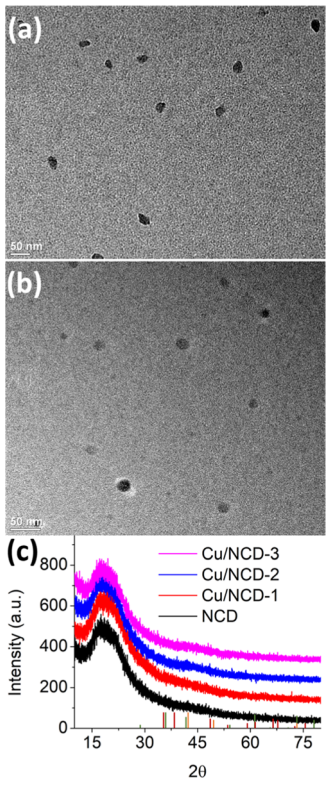

Figure 1. Representative TEM images of (a) NCD and (b) Cu/NCD-3. Scale bars are both 50 nm. (c) XRD patterns of NCD (black), Cu/NCD-1 (red), Cu/NCD-2 (blue), and Cu/NCD-3 (magenta). Reference XRD patterns are provided along the *X*-axis for copper (orange, 00-001-1241), CuO (dark red, 00-002-1040), and Cu_2O (green, 00-003-0892).

This notion is further confirmed in XRD measurements. From the XRD patterns in Figure 1c, one can see that within the 2θ range of 10−80°, all samples display only a single broad peak centered at 2θ = 18°, which is a characteristic of amorphous carbon including the combination of sp^2 and sp^3 carbons.[40] The lack of any other diffraction features in the XRD patterns suggests the absence of crystalline particles containing copper metal or copper oxide within the produced materials. This is consistent with the absence of lattice fringes observed in TEM measurements (Figure S2).

The elemental compositions and valence states of the samples were then examined by XPS measurements. In the survey scans (Figure S4), the elements of C, O, and N can be readily identified in all samples, with Cu also in Cu/NCD-1, Cu/NCD-2, and Cu/NCD-3. The absence of other elements suggests the high purity of the samples. Figure 2a depicts the corresponding high-resolution XPS spectra of the C 1s electrons. Deconvolution yields three components for all samples, (green) sp^2 carbon at ca. 284.5 eV, (orange) sp^3 carbon at 285.6 eV, and (purple) oxidized carbon (i.e., COOH, C═O) at 287.5 eV (Table S1). Notably, the sp^2 carbon content is found to increase with increasing Cu(acac)$_2$ feed from 36.31 atom % for NCD to 39.18 atom % for Cu/NC-1, 40.32 atom % for Cu/NC-2, and 46.94 atom % for Cu/NC-3; and the Csp^2/Csp^3 ratio increases accordingly from 2.4

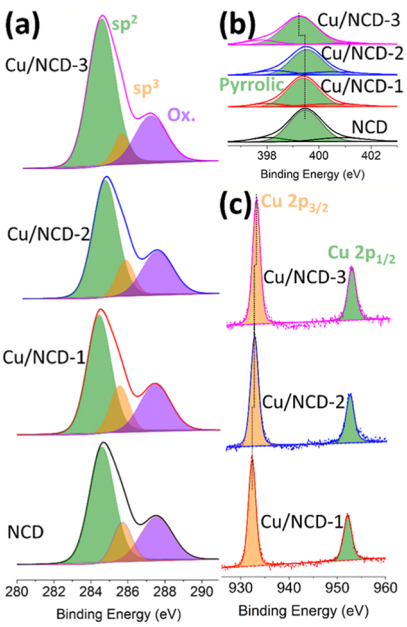

Figure 2. High-resolution XPS spectra of (a) C 1s, (b) N 1s, and (c) Cu 2p electrons of the NCD and Cu/NCD samples. Solid curves are experimental data, and shaded peaks are deconvolution fits.

https://dx.doi.org/10.1021/acs.langmuir.0c02293
Langmuir 2020, 36, 11629−11636

to 3.3, 3.4, and 7.3, respectively, whereas the amount of oxidized carbon remains relatively constant among the entire series of samples (Table S2). This implies enhanced graphitization of citric acid and melamine by $Cu(acac)_2$ under the thermal conditions.

Figure 2b depicts the high-resolution XPS spectra of the N 1s electrons. For the NCD sample, deconvolution yields a primary peak (shaded in green) at 399.3 eV and two minor ones at 398.0 and 400.5 eV, which can be assigned to pyrrolic, pyridinic, and graphitic N, respectively (Table S1).[41,42] This suggests successful doping of N into the carbon skeleton. With the addition of $Cu(acac)_2$ in sample preparation, the binding energies of these peaks remain virtually unchanged, likely because of the low contents of the Cu dopants (Table S2). In addition, the N dopant concentrations were found to be rather consistent among the samples, at 15.24 atom % for NCD, 13.44 atom % for Cu/NCD-1, 13.00 atom % for Cu/NCD-2, and 15.61 atom % for Cu/NCD-3 (Table S2).

The high-resolution XPS scans of the Cu 2p electrons are shown in Figure 2c. One can see that for the Cu/NCD samples, two well-defined peaks can be resolved, at 932.2 and 952.0 eV for Cu/NCD-1, 932.3 and 952.1 eV for Cu/NCD-2, and 932.4 and 952.2 eV for Cu/NCD-3, with a spin−orbit coupling of Δ = 19.8 eV (Table S1).[43] These can be assigned to the $2p_{3/2}$ (orange) and $2p_{1/2}$ (green) electrons of Cu(I) (further confirmed in UV−vis absorption measurements, vide infra), as the lack of well-defined satellite peaks rules out the formation of Cu(II) species.[44] This suggests (partial) reduction of Cu^{2+} in the thermal synthesis of the samples, yet the degree of reduction became lesser with increasing $Cu(acac)_2$ feed, as manifested by a slight increase of the Cu $2p_{3/2}$ binding energy from Cu/NCD-1 to Cu/NCD-3 (Table S1).[45] Furthermore, the copper content within the samples was found to be very low, only 1.57 wt % (0.32 atom %) for Cu/CND-1, 1.07 wt % (0.22 atom %) for Cu/CND-2, and 1.09 wt % (0.22 atom %) for Cu/CND-3 (Table S2). Consistent results were obtained in ICP-OES measurements, where the copper loading was estimated to be 1.55 wt % for Cu/NCD-1, 1.06 wt %, for Cu/NCD-2, and 1.12 wt % for Cu/NCD-3. A comparison between the XPS and ICP-OES results can be seen in Figure S5.

The optical properties of the samples were then examined by UV−vis and photoluminescence spectroscopy measurements. Figure 3a depicts the normalized UV−vis and SSPL spectra for the series of samples. In the UV−vis absorption measurements, all samples exhibit a primary absorption peak centered at ca. 335 nm, which can be attributed to the n → π^* transitions of the C═O, C═C, and C═N moieties in the carbon dots that have been identified in XPS measurements (Figure 2).[46] In SSPL measurements, all samples display a pair of well-defined excitation and emission peaks, at λ_{ex} = 372 nm and λ_{em} = 451 nm for NCD, 364 and 430 nm for Cu/NCD-1, 366 and 435 nm for Cu/NCD-2, and 372 and 450 nm for Cu/NCD-3. One can see that the normalized photoluminescence intensity is apparently quenched with the incorporation of copper into the carbon scaffold, by 37% for Cu/NCD-1, 53% for Cu/NCD-2, and 42% for Cu/NCD-3.[47] Note that in the copper-free carbon dots, the photoluminescence most likely arose from the C═O and C═N functional moieties,[35,36] whereas in the Cu/NCD samples, it is probably the Cu−N coordination structure that was responsible for the emission.[33] In fact, by subtracting the UV−vis absorption spectrum of NCD from those of the Cu/NCD samples, the resulting difference spectra exhibited

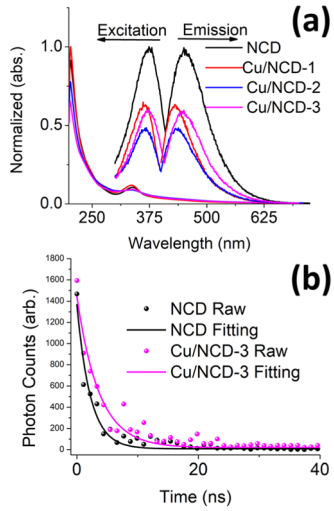

Figure 3. (a) UV−vis and SSPL spectra of NCD (black), Cu/CND-1 (red), Cu/CND-2 (blue), and Cu/CND-3 (magenta). The UV−vis spectra are normalized to the respective absorbance at 203 nm, and the fluorescence spectra are normalized to the corresponding optical absorbance at the excitation wavelength and then normalized to the emission intensity of the NCD sample. All measurements are performed in 1× PBS. (b) TRPL emission spectra at the excitation of 365 nm for the NCD and Cu/NCD-3 samples. Symbols are experimental data and solid curves are exponential fits.

multiple peaks within the range of 400−650 nm (Figure S6), which are characteristic of the Cu−N moieties in conventional copper(I)−pyrrole/pyridine complexes.[48−50] The fact that the NCD sample exhibited a markedly higher quantum yield than the Cu/NCD series suggests more facile recombination of photogenerated electron−hole pairs in the former.

Consistent behaviors were observed in TRPL measurements. Figure 3b depicts the TRPL profiles of NCD (black) and Cu/NCD-3 (magenta) after pulsed laser excitation at 365 nm, which were fitted to single-exponential decay kinetics, $I(t) = Ae^{-t/\tau}$. The calculated decay time constant (τ) was estimated to be 2.2 ns for NCD and 3.6 ns for Cu/NCD-3. The extended lifetime from 2.2 to 3.6 ns with the addition of copper is in good agreement with diminished emission observed above in SSPL measurements and results reported in previous studies.[51,52] This prolonged lifetime is conducive to the separation of photogenerated electron−hole pairs, leading to enhanced performance in ROS production (vide infra).

To quantify the antibacterial properties of the produced materials, a series of photodynamic experiments were performed under photoirradiation with the peak wavelength at 365 nm, as shown in Figure 4a. Two control experiments were also included for comparison, one with *E. coli* alone (light green) and the other with $CuCl_2$ (orange) at a copper concentration equivalent to that of Cu/NCD-3. The corresponding photographs of the colonies grown on LB agar plates are shown in Figures 4b and S7. There are three aspects that warrant special attention. (i) In the two control experiments, no appreciable loss in CFUs was observed after 7 min of photoirradiation. (ii) NCD led to only a minimal loss of bacterial growth. (iii) Apparent photoinduced antibacterial activity can be seen with the Cu/NCD series, and the activity increased in the order NCD < Cu/NCD-1 < Cu/NCD-2 < Cu/NCD-3, highlighting the importance of copper dispersion into the carbon dots to the bactericidal action. For instance, among the series of samples, a complete loss of all CFUs can

https://dx.doi.org/10.1021/acs.langmuir.0c02293
Langmuir 2020, 36, 11629−11636

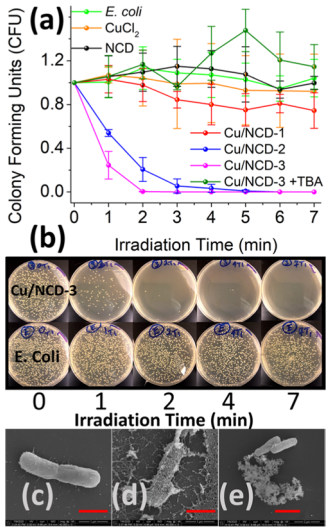

Figure 4. (a) Antibacterial studies under photoirradiation at the peak wavelength at 365 nm. Two control samples are included: *E. coli* alone in 1× PBS (light green), and $CuCl_2$ in 1× PBS (orange) at a concentration equivalent to that of Cu/NCD-3 (12.8 ppm). A second sample of Cu/NCD-3 is tested in the presence of a hydroxyl radical quencher, TBA at 10 mg L^{-1} (dark green). All samples have been tested in triplicate, and the data points display the corresponding average and standard deviation. (b) Photographs depicting *E. coli* grown on LB agar plates at different photoirradiation time points (0, 1, 2, 4, and 7 min) in the absence (bottom) and presence (top) of Cu/NCD-3. SEM images of (c) *E. coli* control, (d) *E. coli* with Cu/NCD-3 after photoirradiation, for 7 min, and (e) *E. coli* with Cu/NCD-3 in the dark. The scale bars indicated in red are 1, 1, and 2 μm, respectively.

be seen after 6 min of photoirradiation with Cu/NCD-2 and only 2 min with Cu/NCD-3, whereas the appreciable growth of bacteria can still be seen with NCD and Cu/NCD-1. This suggests that Cu/NCD-3 possesses the greatest photoinduced antibacterial activity among all samples. This coincides with the longest lifetime of photogenerated electron−hole pairs of the sample, as demonstrated in TRPL measurements, suggesting that the Cu−N moieties likely facilitated the separation of the electron−hole pairs and the subsequent formation of ROS. Additional contributions may arise from the high Csp^2/Csp^3 ratio in Cu/NCD-3 that facilitated charge migration within the carbon dots. These results also suggest that copper leaching, if any, does not make any meaningful contribution to the antimicrobial activity.

The difference of the bactericidal activity can also be readily visualized in SEM measurements of the bacterial cell morphologies. From Figure 4c−e, one can see that the *E. coli* cells sustained significant membrane damages in the presence of Cu/NCD-3 under photoirradiation for 7 min (panel d), whereas in the dark, the cell morphology remained largely intact (panel e), in comparison to the control (panel c).

Notably, Cu/NCD-3 lost all bactericidal activity in the presence of a common hydroxyl radical scavenger, TBA (Figures 4a and S7), suggesting that hydroxyl radicals were responsible for the antimicrobial activity of Cu/NCD-3, which are generally produced by the photoreduction of oxygen and/or photodissociation of water.[8,53,54] A similar trend was observed when a common Gram-positive strain of bacteria, *S. epidermidis*, was used in place of *E. coli* under otherwise identical experimental conditions. Results from this Gram-positive test are shown in Figure S8.

It is interesting to note that no apparent antimicrobial activity was observed with NCD or Cu/NCD in the dark. Figure 5 depicts the corresponding *E. coli* growth curves

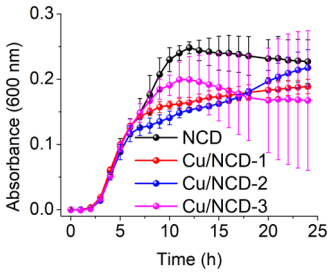

Figure 5. Bacterial growth curves in the dark. Each measurement is repeated in triplicate, with 1× PBS as the solvent. Sample concentrations are all 600 μg mL^{-1}, identical to those in photodynamic experiments in Figure 4.

acquired in the dark. The growth rates during the log phase growth, between 3 and 6 h of incubation, in essence, show little to no change between the samples and between trials. This suggests that bacterial growth in the absence of photoirradiation is unaffected by the presence of the NCD or Cu/NCD samples. These findings are consistent with the notion that photoirradiation plays a critical role in the antibacterial activity of the carbon dots.

Fluorescence microscopy studies were then carried out to quantify the intracellular ROS generation using CellROX green as the fluorescence probe. Note that CellROX green is commonly utilized to measure the oxidative stress of living cells. It is nonfluorescent in the reduced state but may bind to DNA and emit green fluorescence upon oxidation by, for instance, ROS. Thus, it may be used to visualize ROS production during bactericidal actions. Figure 6 shows the

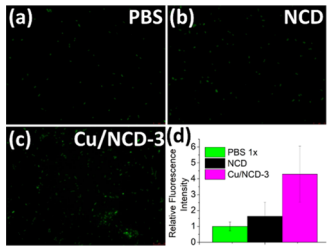

Figure 6. Representative fluorescence micrographs of *E. coli* cells stained with CellROX green after 1 min of photoirradiation at a peak wavelength between 395 and 400 nm in the presence of (a) PBS only, (b) NCD (600 μg mL^{-1} in PBS), and Cu/NCD-3 (600 μg mL^{-1} in PBS). (d) Bar charts of the average fluorescence intensity of the bacterial cells after photoirradiation.

representative fluorescence micrographs of the *E. coli* cells stained with CellROX green after 1 min of photoirradiation (395−400 nm) in (a) PBS only (as a control), (b) NCD, and (c) Cu/NCD-3. One can see that the green dots are far more abundant and intense in panel (c) than in panels (a) and (b). Figure 6d shows the graphical representation of the fluorescence intensity for each sample averaged over three ROIs for PBS alone (green), NCD (black), and Cu/NCD-3 (magenta). One can see that there is no significant statistical difference in the fluorescence intensity between the PBS

https://dx.doi.org/10.1021/acs.langmuir.0c02293
Langmuir 2020, 36, 11629−11636

control and NCD, suggesting a minimal contribution from the carbon dots alone to the photogeneration of ROS. By contrast, Cu/NCD-3 exhibited a fluorescence intensity that was almost fourfold greater than those of the other two samples. This confirms the notion that ROS production was greatly facilitated by the atomic dispersion of Cu into the NCD skeleton, and such enhanced photocatalytic activity led to a marked improvement of the antibacterial activity of Cu/NCD-3, which was likely aided by the enrichment of bacterial cells around the carbon dots (Figure S9).

CONCLUSIONS

Carbon dots doped with Cu−N coordination moieties were readily prepared by a solid-state thermal process, with the particle size ranging from 12 to 37 nm in diameter. Copper was found to be in the Cu(I) oxidation state with no apparent copper crystallinity, and the loadings ranged from 1.07 to 1.57 wt %. Photoluminescence studies showed that the atomic dispersion of copper centers into the carbon dots markedly quenched the emission and prolonged the photoluminescence lifetime. The photoinduced antibacterial activity was found to increase in the order NCD < Cu/NCD-1 < Cu/NCD-2 < Cu/NCD-3, which is consistent with an increase of the sp^2 carbon content. This may be due to improved photoinduced electron−hole pair migration and separation leading to hydroxyl radical formation, as evidenced in fluorescence microscopic studies with CellROX green as the probe and control experiments using TBA as the hydroxyl radical scavenger. The produced materials were found to have little to no effect on bacterial growth in the absence of photoirradiation. These functional nanocomposites may see important applications in wound care devices and may help alleviate the current role of β-lactam-based antibiotics.

ASSOCIATED CONTENT

Supporting Information

The Supporting Information is available free of charge at https://pubs.acs.org/doi/10.1021/acs.langmuir.0c02293.

Additional experimental data, XPS binding energy and atomic percentage of the various elements, core size histogram, high-resolution TEM images, STEM image and EELS spectrum, XPS survey scans, comparison of copper wt%, UV−vis difference spectra, photographs of incubated LB agar plates, Gram-positive antibacterial studies, and *E. coli* growth curves (PDF)

AUTHOR INFORMATION

Corresponding Authors

Shaowei Chen − *Department of Chemistry and Biochemistry, University of California, Santa Cruz, California 95064, United States*; orcid.org/0000-0002-3668-8551; Email: shaowei@ucsc.edu

Chad Saltikov − *Department of Microbiology and Environmental Toxicology, University of California, Santa Cruz, California 95064, United States*; Email: saltikov@ucsc.edu

Authors

Forrest Nichols − *Department of Chemistry and Biochemistry, University of California, Santa Cruz, California 95064, United States*

Jia En Lu − *Department of Chemistry and Biochemistry, University of California, Santa Cruz, California 95064, United States*

Rene Mercado − *Department of Chemistry and Biochemistry, University of California, Santa Cruz, California 95064, United States*

Mauricio D. Rojas-Andrade − *Department of Chemistry and Biochemistry, University of California, Santa Cruz, California 95064, United States*

Shunlian Ning − *School of Environment and Energy, South China University of Technology, Guangzhou 510006, China*

Zahra Azhar − *Department of Chemistry and Biochemistry, University of California, Santa Cruz, California 95064, United States*

Jasleen Sandhu − *Department of Chemistry and Biochemistry, University of California, Santa Cruz, California 95064, United States*

Rafael Cazares − *Department of Chemistry and Biochemistry, University of California, Santa Cruz, California 95064, United States*

Complete contact information is available at: https://pubs.acs.org/10.1021/acs.langmuir.0c02293

Author Contributions

The manuscript was written through the contribution of all authors. All authors have given approval to the final version of the manuscript.

Notes

The authors declare no competing financial interest.

ACKNOWLEDGMENTS

The authors thank Dr. Chengyu Song for the assistance in STEM and elemental mapping measurements. This work is supported, in part, by the National Science Foundation (CBET-1848841 and CHE-1900235). TEM and XPS work was carried out at the National Center for Electron Microscopy and Molecular Foundry of Lawrence Berkeley National Laboratory, which is supported by the Office of Science, Office of Basic Energy Sciences, of the US Department of Energy under Contract No. DE-AC02-05CH11231, as part of a user project.

REFERENCES

(1) Zheng, K. Y.; Setyawati, M. I.; Leong, D. T.; Xie, J. P. Antimicrobial silver nanomaterials. *Coord. Chem. Rev.* **2018**, *357*, 1−17.

(2) Piddock, L. J. V. The crisis of no new antibiotics—what is the way forward? *Lancet Infect. Dis.* **2012**, *12*, 249−253.

(3) Klein, E. Y.; Van Boeckel, T. P.; Martinez, E. M.; Pant, S.; Gandra, S.; Levin, S. A.; Goossens, H.; Laxminarayan, R. Global increase and geographic convergence in antibiotic consumption between 2000 and 2015. *Proc. Natl. Acad. Sci. U.S.A.* **2018**, *115*, E3463−E3470.

(4) Partridge, S. R.; Kwong, S. M.; Firth, N.; Jensen, S. O. Mobile Genetic Elements Associated with Antimicrobial Resistance. *Clin. Microbiol. Rev.* **2018**, *31*, No. e00088-17.

(5) Bush, K.; Bradford, P. A. Interplay between β-lactamases and new β-lactamase inhibitors. *Nat. Rev. Microbiol.* **2019**, *17*, 295−306.

(6) Kumar, R.; Umar, A.; Kumar, G.; Nalwa, H. S. Antimicrobial properties of ZnO nanomaterials: A review. *Ceram. Int.* **2017**, *43*, 3940−3961.

(7) Qi, K. Z.; Cheng, B.; Yu, J. G.; Ho, W. K. Review on the improvement of the photocatalytic and antibacterial activities of ZnO. *J. Alloys Compd.* **2017**, *727*, 792−820.

(8) Nosaka, Y.; Nosaka, A. Y. Generation and Detection of Reactive Oxygen Species in Photocatalysis. *Chem. Rev.* **2017**, *117*, 11302−11336.
(9) Dwyer, D. J.; Kohanski, M. A.; Collins, J. J. Role of reactive oxygen species in antibiotic action and resistance. *Curr. Opin. Microbiol.* **2009**, *12*, 482−489.
(10) He, T.; Peng, Y.; Li, Q.; Lu, J. E.; Liu, Q.; Mercado, R.; Chen, Y.; Nichols, F.; Zhang, Y.; Chen, S. Nanocomposites Based on Ruthenium Nanoparticles Supported on Cobalt and Nitrogen-Codoped Graphene Nanosheets as Bifunctional Catalysts for Electrochemical Water Splitting. *ACS Appl. Mater. Interfaces* **2019**, *11*, 46912−46919.
(11) Yang, W.; Chata, G.; Zhang, Y.; Peng, Y.; Lu, J. E.; Wang, N.; Mercado, R.; Li, J.; Chen, S. Graphene oxide-supported zinc cobalt oxides as effective cathode catalysts for microbial fuel cell: High catalytic activity and inhibition of biofilm formation. *Nano Energy* **2019**, *57*, 811−819.
(12) Wang, N.; Li, L.; Zhou, N.; Chen, S. Cage Breaking of C60 Into Photoluminescent Graphene Oxide Quantum Dots: An Efficient Peroxidase Mimic. *Phys. Status Solidi B* **2018**, *255*, No. 1700535.
(13) Chen, L.; Peng, Y.; Lu, J.-E.; Wang, N.; Hu, P.; Lu, B.; Chen, S. Platinum nanoparticles encapsulated in nitrogen-doped graphene quantum dots: Enhanced electrocatalytic reduction of oxygen by nitrogen dopants. *Int. J. Hydrogen Energy* **2017**, *42*, 29192−29200.
(14) Deming, C. P.; Mercado, R.; Lu, J. E.; Gadiraju, V.; Khan, M.; Chen, S. Oxygen electroreduction catalyzed by palladium nanoparticles supported on nitrogen-doped graphene quantum dots: impacts of nitrogen dopants. *ACS Sustainable Chem. Eng.* **2016**, *4*, 6580−6589.
(15) Lu, B.; Guo, L.; Wu, F.; Peng, Y.; Lu, J. E.; Smart, T. J.; Wang, N.; Finfrock, Y. Z.; Morris, D.; Zhang, P.; Li, N.; Gao, P.; Ping, Y.; Chen, S. Ruthenium atomically dispersed in carbon outperforms platinum toward hydrogen evolution in alkaline media. *Nat. Commun.* **2019**, *10*, No. 631.
(16) Rojas-Andrade, M. D.; Chata, G.; Rouholiman, D.; Liu, J.; Saltikov, C.; Chen, S. Antibacterial mechanisms of graphene-based composite nanomaterials. *Nanoscale* **2017**, *9*, 994−1006.
(17) Liu, J.; Rojas-Andrade, M. D.; Chata, G.; Peng, Y.; Roseman, G.; Lu, J.-E.; Millhauser, G. L.; Saltikov, C.; Chen, S. Photo-enhanced antibacterial activity of ZnO/graphene quantum dot nanocomposites. *Nanoscale* **2018**, *10*, 158−166.
(18) Rojas-Andrade, M. D.; Nguyen, T. A.; Mistler, W. P.; Armas, J.; Lu, J. E.; Roseman, G.; Hollingsworth, W. R.; Nichols, F.; Millhauser, G.; Ayzner, A. L.; et al. Antimicrobial activity of graphene oxide quantum dots: impacts of chemical reduction. *Nanoscale Adv.* **2020**, *2*, 1074−1083.
(19) Azimirad, R.; Safa, S. Photocatalytic and Antifungal Activity of Flower-Like Copper Oxide Nanostructures. *Synth. React. Inorg., Met.-Org., Nano-Met. Chem.* **2014**, *44*, 798−803.
(20) Katwal, R.; Kaur, H.; Sharma, G.; Naushad, M.; Pathania, D. Electrochemical synthesized copper oxide nanoparticles for enhanced photocatalytic and antimicrobial activity. *J. Ind. Eng. Chem.* **2015**, *31*, 173−184.
(21) Leyland, N. S.; Podporska-Carroll, J.; Browne, J.; Hinder, S. J.; Quilty, B.; Pillai, S. C. Highly Efficient F, Cu doped TiO_2 antibacterial visible light active photocatalytic coatings to combat hospital-acquired infections. *Sci. Rep.* **2016**, *6*, No. 24770.
(22) Ray, S. K.; Dhakal, D.; Kshetri, Y. K.; Lee, S. W. Cu-alpha-$NiMoO_4$ photocatalyst for degradation of Methylene blue with pathways and antibacterial performance. *J. Photochem. Photobiol., A* **2017**, *348*, 18−32.
(23) Rtimi, S.; Dionysiou, D. D.; Pillai, S. C.; Kiwi, J. Advances in catalytic/photocatalytic bacterial inactivation by nano Ag and Cu coated surfaces and medical devices. *Appl. Catal., B* **2019**, *240*, 291−318.
(24) Xiong, L. B.; Yu, H. Q.; Nie, C. J.; Xiao, Y. J.; Zeng, Q. D.; Wang, G. J.; Wang, B. Y.; Lv, H.; Li, Q. G.; Chen, S. S. Size-controlled synthesis of Cu_2O nanoparticles: size effect on antibacterial activity and application as a photocatalyst for highly efficient H_2O_2 evolution. *RSC Adv.* **2017**, *7*, 51822−51830.
(25) Yadav, H. M.; Otari, S. V.; Koli, V. B.; Mali, S. S.; Hong, C. K.; Pawar, S. H.; Delekar, S. D. Preparation and characterization of copper-doped anatase TiO2 nanoparticles with visible light photocatalytic antibacterial activity. *J. Photochem. Photobiol., A* **2014**, *280*, 32−38.
(26) Yordanova, S.; Temiz, H. T.; Boyaci, I. H.; Stoyanov, S.; Vasileva-Tonkova, E.; Asiri, A.; Grabchev, I. Synthesis, characterization and in vitro antimicrobial activity of a new blue fluorescent Cu(II) metal complex of bis-1,8-naphthalimide. *J. Mol. Struct.* **2015**, *1101*, 50−56.
(27) Bagihalli, G. B.; Avaji, P. G.; Patil, S. A.; Badami, P. S. Synthesis, spectral characterization, in vitro antibacterial, antifungal and cytotoxic activities of Co(II), Ni(II) and Cu(II) complexes with 1,2,4-triazole Schiff bases. *Eur. J. Med. Chem.* **2008**, *43*, 2639−2649.
(28) Qi, L. F.; Xu, Z. R.; Jiang, X.; Hu, C. H.; Zou, X. F. Preparation and antibacterial activity of chitosan nanoparticles. *Carbohydr. Res.* **2004**, *339*, 2693−2700.
(29) Ruparelia, J. P.; Chatterjee, A. K.; Duttagupta, S. P.; Mukherji, S. Strain specificity in antimicrobial activity of silver and copper nanoparticles. *Acta Biomater.* **2008**, *4*, 707−716.
(30) Stanić, V.; Dimitrijevic, S.; Antic-Stankovic, J.; Mitric, M.; Jokic, B.; Plecas, I. B.; Raicevic, S. Synthesis, characterization and antimicrobial activity of copper and zinc-doped hydroxyapatite nanopowders. *Appl. Surf. Sci.* **2010**, *256*, 6083−6089.
(31) Gaetke, L. M.; Chow, C. K. Copper toxicity, oxidative stress, and antioxidant nutrients. *Toxicology* **2003**, *189*, 147−163.
(32) Gong, N.; Ma, X.; Ye, X.; Zhou, Q.; Chen, X.; Tan, X.; Yao, S.; Huo, S.; Zhang, T.; Chen, S.; et al. Carbon-dot-supported atomically dispersed gold as a mitochondrial oxidative stress amplifier for cancer treatment. *Nat. Nanotechnol.* **2019**, *14*, 379.
(33) Peng, Y.; Lu, B. Z.; Chen, L. M.; Wang, N.; Lu, J. E.; Ping, Y.; Chen, S. W. Hydrogen evolution reaction catalyzed by ruthenium ion-complexed graphitic carbon nitride nanosheets. *J. Mater. Chem. A* **2017**, *5*, 18261−18269.
(34) Peng, Y.; Pan, W. Z.; Wang, N.; Lu, J. E.; Chen, S. W. Ruthenium Ion-Complexed Graphitic Carbon Nitride Nanosheets Supported on Reduced Graphene Oxide as High-Performance Catalysts for Electrochemical Hydrogen Evolution. *ChemSusChem* **2018**, *11*, 130−136.
(35) Tian, L.; Ghosh, D.; Chen, W.; Pradhan, S.; Chang, X.; Chen, S. Nanosized Carbon Particles From Natural Gas Soot. *Chem. Mater.* **2009**, *21*, 2803−2809.
(36) Tian, L.; Song, Y.; Chang, X.; Chen, S. Hydrothermally enhanced photoluminescence of carbon nanoparticles. *Scr. Mater.* **2010**, *62*, 883−886.
(37) Jiang, L.; Yuan, X.; Pan, Y.; Liang, J.; Zeng, G.; Wu, Z.; Wang, H. Doping of graphitic carbon nitride for photocatalysis: a reveiw. *Appl. Catal., B* **2017**, *217*, 388−406.
(38) Iqbal, A.; Iqbal, K.; Xu, L.; Li, B.; Gong, D.; Liu, X.; Guo, Y.; Liu, W.; Qin, W.; Guo, H. Heterogeneous synthesis of nitrogen-doped carbon dots prepared via anhydrous citric acid and melamine for selective and sensitive turn on-off-on detection of Hg (II), glutathione and its cellular imaging. *Sens. Actuators, B* **2018**, *255*, 1130−1138.
(39) Liu, J.; Shao, J.; Wang, Y.; Li, J.; Liu, H.; Wang, A.; Hui, A.; Chen, S. Antimicrobial Activity of Zinc Oxide−Graphene Quantum Dot Nanocomposites: Enhanced Adsorption on Bacterial Cells by Cationic Capping Polymers. *ACS Sustainable Chem. Eng.* **2019**, *7*, 16264−16273.
(40) Lee, H.-M.; Kang, H.-R.; An, K.-H.; Kim, H.-G.; Kim, B.-J. Comparative studies of porous carbon nanofibers by various activation methods. *Carbon Lett.* **2013**, *14*, 180−185.
(41) Titantah, J. T.; Lamoen, D. Carbon and nitrogen 1s energy levels in amorphous carbon nitride systems: XPS interpretation using first-principles. *Diamond Relat. Mater.* **2007**, *16*, 581−588.
(42) Akada, K.; Terasawa, T.-o.; Imamura, G.; Obata, S.; Saiki, K. Control of work function of graphene by plasma assisted nitrogen doping. *Appl. Phys. Lett.* **2014**, *104*, No. 131602.

https://dx.doi.org/10.1021/acs.langmuir.0c02293
Langmuir 2020, 36, 11629−11636

(43) Xia, J.; Xu, Y.; Hu, B.; Lin, J. A rapid approach to urushiol–copper (I) coordination polymer under UV irradiation. *Prog. Org. Coat.* **2009**, *65*, 510–513.
(44) Brettholle, M.; Hoefft, O.; Klarhöfer, L.; Mathes, S.; Maus-Friedrichs, W.; El Abedin, S. Z.; Krischok, S.; Janek, J.; Endres, F. Plasma electrochemistry in ionic liquids: deposition of copper nanoparticles. *Phys. Chem. Chem. Phys.* **2010**, *12*, 1750–1755.
(45) Peng, Y.; Lu, B. Z.; Wang, N.; Li, L. G.; Chen, S. W. Impacts of interfacial charge transfer on nanoparticle electrocatalytic activity towards oxygen reduction. *Phys. Chem. Chem. Phys.* **2017**, *19*, 9336–9348.
(46) Chen, L.; Hu, P.; Deming, C. P.; Wang, N.; Lu, J. E.; Chen, S. Intervalence Charge Transfer of Ruthenium–Nitrogen Moieties Embedded within Nitrogen-Doped Graphene Quantum Dots. *J. Phys. Chem. C* **2016**, *120*, 13303–13309.
(47) Wang, F.; Gu, Z.; Lei, W.; Wang, W.; Xia, X.; Hao, Q. Graphene quantum dots as a fluorescent sensing platform for highly efficient detection of copper(II) ions. *Sens. Actuators, B* **2014**, *190*, 516–522.
(48) Tümer, F.; Köse, M.; Tümer, M.; Güngör, S. A.; Şahin, S. Absorption, redox and aggregation properties of new α,α-diaminoporphyrin based ligands and their Cu(II) complexes. *J. Mol. Struct.* **2019**, *1190*, 148–159.
(49) Kantekin, H.; Saka, E. T.; Ertem, B.; Mısır, M. N.; Yalazan, H.; Sarkı, G. New peripherally tetra-[trans-3, 7-dimethyl-2, 6-octadien-1-ol] substituted metallophthalocyanines: synthesis, characterization and catalytic activity studies on the oxidation of phenolic compounds. *J. Coord. Chem.* **2018**, *71*, 164–182.
(50) Kim, E.; Helton, M. E.; Wasser, I. M.; Karlin, K. D.; Lu, S.; Huang, H.-w.; Moënne-Loccoz, P.; Incarvito, C. D.; Rheingold, A. L.; Honecker, M.; et al. Superoxo, μ-peroxo, and μ-oxo complexes from heme/O_2 and heme-Cu/O_2 reactivity: Copper ligand influences in cytochrome c oxidase models. *Proc. Natl. Acad. Sci. U.S.A.* **2003**, *100*, 3623–3628.
(51) Kollmannsberger, M.; Rurack, K.; Resch-Genger, U.; Daub, J. Ultrafast Charge Transfer in Amino-Substituted Boron Dipyrromethene Dyes and Its Inhibition by Cation Complexation: A New Design Concept for Highly Sensitive Fluorescent Probes. *J. Phys. Chem. A* **1998**, *102*, 10211–10220.
(52) Peng, Y.; Lu, B.; Wu, F.; Zhang, F.; Lu, J. E.; Kang, X.; Ping, Y.; Chen, S. Point of Anchor: Impacts on Interfacial Charge Transfer of Metal Oxide Nanoparticles. *J. Am. Chem. Soc.* **2018**, *140*, 15290–15299.
(53) Chen, C.-Y.; Jafvert, C. T. Photoreactivity of Carboxylated Single-Walled Carbon Nanotubes in Sunlight: Reactive Oxygen Species Production in Water. *Environ. Sci. Technol.* **2010**, *44*, 6674–6679.
(54) Milligan, J. R.; Ward, J. F. Yield of single-strand breaks due to attack on DNA by scavenger-derived radicals. *Radiat. Res.* **1994**, *137*, 295–299.

https://dx.doi.org/10.1021/acs.langmuir.0c02293
Langmuir 2020, 36, 11629–11636